Journal of the European Ceramic Society xxx (xxxx) xxx–xxx

Contents lists available at ScienceDirect

Journal of the European Ceramic Society

journal homepage: www.elsevier.com/locate/jeurceramsoc

Original Article

Ferroelastic domain structure and phase transition in single-crystalline $[PbZn_{1/3}Nb_{2/3}O_3]_{1-x}[PbTiO_3]_x$ observed via *in situ* x-ray microbeam

Tao Li[a,b,c], Zehui Du[d], Nobumichi Tamura[e], Mao Ye[a,b,c], Saikumar Inguva[a,b], Wei Lu[f], Xierong Zeng[a,b], Shanming Ke[a,*], Haitao Huang[c,*]

[a] Shenzhen Key Laboratory of Special Functional Materials, Shenzhen Engineering Laboratory for Advanced Technology of Ceramics, College of Materials Science and Engineering, Shenzhen University, Shenzhen, 518060, China
[b] Key Laboratory of Optoelectronic Devices and Systems of Ministry of Education and Guangdong Province, College of Optoelectronic Engineering, Shenzhen University, Shenzhen, 518060, China
[c] Department of Applied Physics and Materials Research Center, The Hong Kong Polytechnic University, Hung Hom, Kowloon, Hong Kong, China
[d] Temasek Laboratories, Nanyang Technological University, 637753, Singapore
[e] Advanced Light Source (ALS), Lawrence Berkeley National Laboratory (LBNL), Berkeley, CA, 94720, USA
[f] University Research Facility in Materials Characterization and Device Fabrication, The Hong Kong Polytechnic University, Hong Kong, China

ABSTRACT

(1-x)$Pb(Zn_{1/3}Nb_{2/3})O_3$-x$PbTiO_3$ ((1-x)PZN-xPT in short) is one of the most important piezoelectric materials. In this work, we extensively investigated (1-x)PZN-xPT (x = 0.07–0.11) ferroelectric single crystals using *in-situ* synchrotron μXRD, complemented by TEM and PFM, to correlate microstructures with phase transitions. The results reveal that (i) at 25 °C, the equilibrium state of (1-x)PZN-xPT is a metastable orthorhombic phase for x = 0.07 and 0.08, while it shows coexistence of orthorhombic and tetragonal phases for x = 0.09 and x = 0.11, with all ferroelectric phases accompanied by ferroelastic domains; (ii) upon heating, the phase transformation in x = 0.07 is Orthorhombic → Monoclinic → Tetragonal → Cubic. The coexistence of ferroelectric tetragonal and paraelectric cubic phases was *in-situ* observed in x = 0.08 above Curie temperature (T_C), and (iii) phase transition can be explained by the evolution of the ferroelectric and ferroelastic domains. These results disclose that (1-x)PZN-xPT are in an unstable regime, which is possible factor for its anomalous dielectric response and high piezoelectric coefficient.

1. Introduction

Relaxor ferroelectric single crystals of $Pb(Zn_{1/3}Nb_{2/3})O_3$-$PbTiO_3$ (PZN-PT) solid solution are considered as next-generation materials for future high-performance transducers, sensors, and actuators due to their superior piezoelectric and electromechanical properties (i.e., d_{33} ~ 2500–3000 pC/N, k_{33} > 92% with a maximum strain > 1.7%) [1,2]. Compared to the commercially available $Pb(Mg_{1/3}Nb_{2/3})O_3$-$PbTiO_3$ (PMN-PT) single crystals, PZN-PT single crystals are superior in (a) achieving uniform composition easily, (b) consistently higher (25–40%) piezoelectric properties, (c) larger coercive fields, (d) 50–100% higher elastic compliance, and (e) 10–20 °C higher depolarization temperature. Earlier theoretical investigations have attributed their excellent properties to presence of a monoclinic (*M*) phase which acts as the bridging phase between the rhombohedral (*R*) and the tetragonal (*T*) phases [3,4]. Despite of this, the existence of the *M* phase remains a subject of many debates. Another explanation for their excellent properties is an adaptive phase model, where the *M* phase diffractions are resulting from those nanoscale twinned *R* and *T* domains [5–9]. A nanoscale twin diffraction theory has been proposed to explain the streaked diffraction pattern observed in the perovskite ferroelectrics, which cannot be fully explained by the conventional diffraction theory. This theory sometimes could be ascribed to the *M* phase [8–11]. However, the nanoscale twin diffraction theory is rarely utilized to interpret the complicated diffraction patterns of relaxor ferroelectric single crystals.

In particular, the existence of nanoscale domains and polar nano regions (PNRs) often lead to the broadening or splitting peaks in the conventional X-ray diffraction method. High resolution synchrotron X-ray diffraction has shown that a new orthorhombic (*O*) phase exists in 0.91PZN-0.09PT near the MPB, i.e. in addition to the known *R* and *T* phases [12]. Measurements on the rhombohedral 0.92PZN-0.08PT samples under an electric field have shown that an *O* phase is irreversibly induced by the applied field, which is an indicative of the close

* Corresponding authors.
E-mail addresses: smke@szu.edu.cn (S. Ke), aphhuang@polyu.edu.hk (H. Huang).

https://doi.org/10.1016/j.jeurceramsoc.2017.11.021
Received 14 September 2017; Received in revised form 8 November 2017; Accepted 9 November 2017

proximity of an *R-O* boundary in the phase diagram [10]. The *O* phase was also identified in (1-x)PZN-xPT (x = 0.08–0.10) ferroelectric single crystals by synchrotron X-ray measurement [13]. However, in the aforementioned work, all the (1-x)PZN-xPT ferroelectric single crystals for tested were poled and then crushed into powders, which might bring uncertainties in the measurement due to the electric field and stress induced ferroelastic phase transitions. An *in-situ* synchrotron micro-beam X-ray diffraction (μXRD) on a single crystal sample is thus highly desirable for an accurate structural analysis with a higher resolution. Additionally, the continuous wavelength white micro-beam synchrotron X-rays can compensate the deficiencies of the monochromatic beam to capture the fine microstructures of the materials.

In order to characterize the nanoscale domain structure, transmission electron microscopy (TEM) is a powerful tool. Direct observation from TEM has shown that the existence of nano twin domains in PMN-PT system [14,15], which is attributed to the *M* phases (M_A, M_B, and M_C) according to XRD [6,7]. In this work, TEM was used as a supplementary technique to identify the local domain structures.

The goal of the present study is to explore the microstructure and phase transition in the (1-x)PZN-xPT single crystals by using a combination of *in-situ* synchrotron polychromatic (white beam) μXRD, high resolution TEM (HR-TEM) and piezoresponse force microscopy (PFM).

2. Experimental details

2.1. Sample preparation

The ferroelectric single crystals referenced in this paper were grown by the top-seeded solution method [16], all samples were cut along the $[001]_{pc}$ direction, and then polished into a size of 5 mm × 5 mm × 0.5 mm and annealed at 500 °C for 2 h. After synchrotron μXRD measurement, vacuum-sputtered gold electrodes were applied to both faces of the samples. To obtain single-domain states, a high-temperature poling approach was used [17]. The ferroelectric single crystals PZN-xPT (x = 0.07–0.11) were poled along their respective $[001]_{pc}$ direction at 120 °C with a 10 kV/cm *E*-field, and then cooled to room temperature under the same *E*-field.

2.2. Characterization

2.2.1. Dielectric and piezoelectric measurements

The temperature dependence of dielectric response was measured by the High Performance Modular Measurement System (Novolcontrol Technologies). Piezoelectric coefficients were determined by the quasi-static d_{33} meter (Institute of Acoustics, CAS, Model ZJ-4AN).

2.2.2. Synchrotron X-ray micro-beam diffraction (μXRD) measurement

The μXRD experiment was conducted on a beamline of 12.3.2 in the Advanced Light Source at Lawrence Berkeley National Laboratory. The beam cross-section area was around 1 × 1 μm^2. After initial alignment and calibration, the samples were attached to a heating element by using a high temperature conductive glue to prevent the sample movement during the heating period. The temperature profile was monitored by two thermocouples, one was attached beneath the sample and another was in contact with the sample surface. The samples were heated in steps above the Curie temperature. In all the cases, the temperature variation was not exceeded ± 5 °C for any temperature step. The sample was mounted on a translation stage with its $(0\ 0\ 1)_{pc}$ face at an angle of ~45° with respect to the horizontal incident beam. A two-dimensional scan along *x*- and *y*-axes (laboratory coordinate system) was performed. The scanning steps along the *x*- and *y*-directions were 25 and 10 μm, respectively, with a total scanned area measured was of 100 × 100 μm^2. At each step, the crystal was exposed to X-rays for 1 s. The diffraction Laue patterns produced by the polychromatic radiation were recorded using a hybrid pixel area detector (DECTRIS Pilatus 1 M) with an active area of 179 mm × 169 mm. The data were analyzed with the XMAS Laue indexing software using a non-linear least-square refinement [18,19]. The refined and fitted diffraction spots constitute over 95% of the whole diffraction spots recorded by the area detector, indicating that a high degree of confidence on the indexing. Geometrical calibration parameters (sample-to-detector distance, detector center positions, detector pitch and yaw) were determined by using a section of the Si substrate. In this procedure, the initial lattice constants of a high symmetry (1-x)PZN-xPT cubic phase at room temperature used were $a = b = c = 4.0585$ Å, which come from the ICSD database.

2.2.3. TEM measurement

TEM specimens were prepared by the standard techniques of grinding, dimpling, and argon-ion-beam thinning. The dark-field and high-resolution TEM (HR-TEM) experiments were performed by a Jeol JEM-2100F STEM, which was operated at 200 kV.

2.2.4. PFM measurement

The domain mapping was obtained by a piezoresponse force microscope (PFM, Asylum Research, Oxford) in AC DART PFM mode. Bruker cantilevers with a resonance frequency of 75 kHz were used to record the topography and phase images, simultaneously.

3. Results and discussions

3.1. Ferroelectric/piezoelectric/dielectric properties

In Fig. 1(a), ferroelectric hysteresis loops of all the referenced ferroelectric single crystals at room temperature are depicted. The domain switching feature of the PZN-PT single crystals is quite different from the $Pb(Mg_{1/3}Nb_{2/3})O_3$-$PbTiO_3$ (PMN-PT) single crystals [1,2]. The trend of remanent polarization (P_r) increases to a maximum value and then it decreases with an increasing PT content, which is due to the multiphase coexistence at the morphotropic phase boundary (MPB) [1–4]. However, the coercive field (E_c) increases with an increasing PT content. This is because of that the PT has a typical tetragonal phase structure. As shown in Fig. 1(b), the piezoelectric coefficient d_{33} of (1-x)

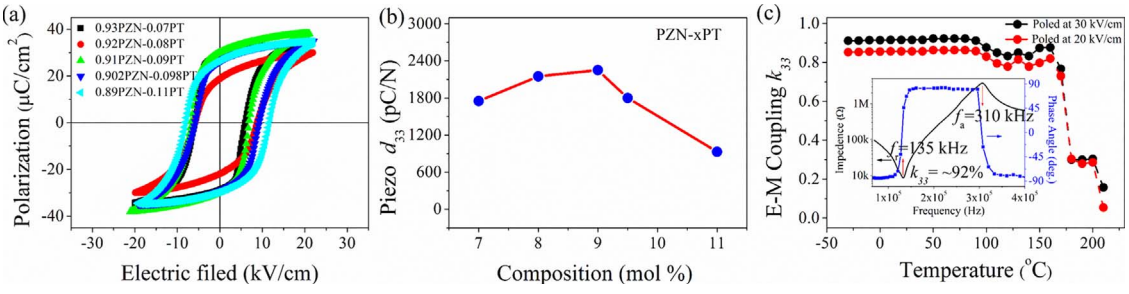

Fig. 1. (a): Room temperature *P-E* hysteresis loops of PZN-xPT (x = 0.07-0.11). (b): The composition dependence of piezoelectric response d_{33} near MPB. (c): The temperature dependence of the longitudinal electromechanical (E-M) coupling factor k_{33} of the x = 0.09 sample poled at different poling fields. Inset of (c) showing the longitudinal impendence spectra and phase angles as a function of frequency based on resonance (f_r) and anti-resonance (f_a) measurement at room temperature.

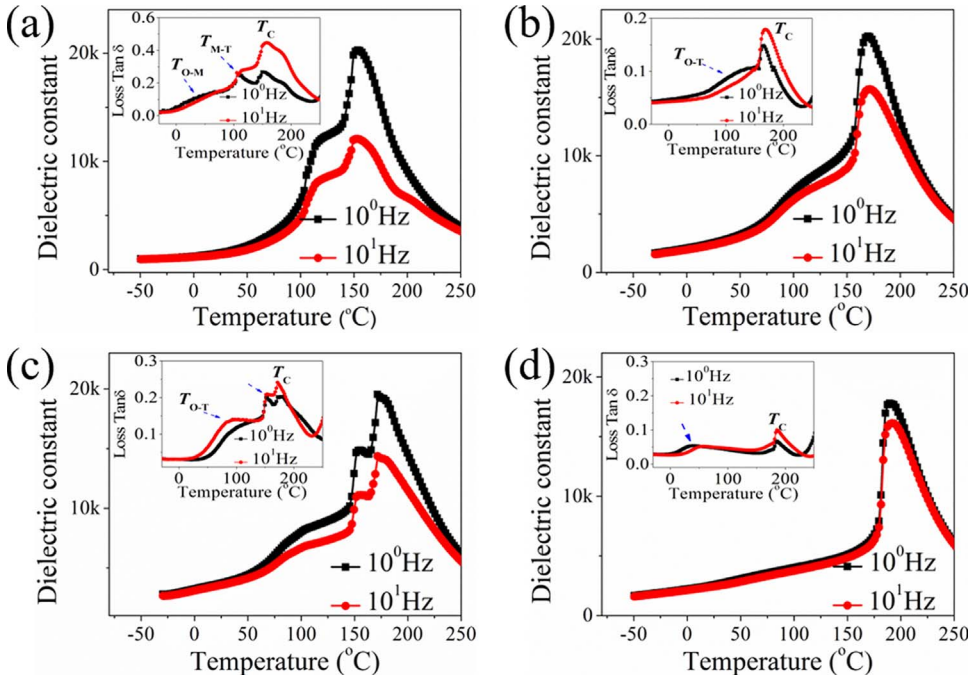

Fig. 2. Dielectric constant and dielectric loss tan δ of $[001]_{pc}$-oriented (1-x)PZN-xPT single crystals as a function of temperature measured at frequencies 10^0 and 10^1 Hz for different compositions, (a): x = 0.07, (b): x = 0.08, (c): x = 0.09, and (d): x = 0.11.

PZN-xPT (x = 0.07–0.11) also shows a maximum value at the MPB composition [13]. Fig. 1(c) presents the variation of the longitudinal electromechanical (E-M) coupling factor k_{33} of x = 0.09 composition as a function of temperature and poling electric fields. The insert of Fig. 1(c) shows the room temperature impedance (at resonance f_r and antiresonance frequencies f_a) and phase angle as a function of frequency at poled electric field of 30 kV/cm, which was calculated k_{33} as a 92% [1,2]. Additionally, it is noteworthy that the longitudinal k_{33} of x = 0.09 was not decreased to zero abruptly at above Curie temperature (T_C), which can be correlated to the polar phase structure components at high temperatures [20]. Fig. 2 shows the temperature dependences of dielectric constant and loss tangent. It revealed the Curie phase transition temperature (T_C) and ferroelectric–ferroelectric phase transition temperature of the each sample [13].

3.2. Ferroelectric domain structure by piezoforce microscopy

Detailed PFM topographic images (as shown in Fig. 3) show a gradual transformation from the hierarchical micro-domains to the maze macro-domains in the (1-x)PZN-xPT single crystals with an increasing x from 0.07 to 0.11. The x = 0.07 sample shows mainly the hierarchical ferroelectric domains with a length from several to tens of microns, and a width of about hundred nanometers (Fig. 3a) [21]. The samples of x = 0.08 and 0.09 show a mixture of hierarchical and maze ferroelectric domains, the number of maze domains increases with an increasing x (Fig. 3b and c). It can be clearly seen that the x = 0.11 sample shows larger maze domain structures (Fig. 3d). Another domain structure features is that the ferroelectric domain boundaries are quite irregular, and these domains are identified as the presence of *M* phases in the PMN-PT single crystals [21–23].

3.3. Phase identification in the (1-x)PZN-xPT single crystals by synchrotron μXRD

Fig. 4 show typical Laue micro-diffraction patterns obtained from the (1-x)PZN-xPT (x = 0.07–011) single crystals at 27 °C corresponding to the crystal structure. Phase identification and crystal orientation are determined by pattern indexing (~0.01° resolution). The indexation of the Laue diffraction patterns identifies that the x = 0.07 and x = 0.08 single crystal samples are purely orthorhombic with *Amm2* space group (Fig. 4a and b), the x = 0.09 sample demonstrates the coexistence of the orthorhombic and tetragonal phases with *Amm2* and *P4 mm* space groups, respectively (Fig. 4c and d). The content of the *T* phase in x = 0.09 sample was calculated to be 35.5%, using an equation: $a = [I_{Tetra.}]/[I_{Tetra.} + I_{Orthor.}]$, where $I_{Tetra.}$ and $I_{Orthor.}$ are the sums of the integrated peak intensities from the *T* and *O* phases, respectively. The x = 0.11 sample mainly present tetragonal phase structure with *P4 mm* space group, but with a minor orthorhombic phase (the indexations of orthorhombic phase is not shown in Fig. 4e and f, but the blue box shows the diffraction peak position of orthorhombic phase). The refined lattice parameters are listed in Table 1.

3.4. Characterization of ferroelastic domains in (1-x)PZN-xPT single crystals by μXRD

In order to achieve a deeper insight into the microstructure structures and the temperature-dependent phase evolutions, the detailed analyses are needed. The crystal uniformity and domain topographic consistency were examined at the first instance. Fig. 5 shows an enlarged view of $\{0\ 0\ l\}_{pc}$ diffraction spots scanned on an area of 100 μm × 100 μm. For each sample, most of the images present similar-shaped diffraction patterns with a little difference, indicating that macroscale uniformity of the crystals. As shown in Figs. 4 and 5, an important observation is that the diffuse scattering occurs in two forms: (A) sharp streaks emanate from Bragg peaks and extend along ⟨001⟩ and ⟨110⟩ directions clearly, which is determined by the cations displaced and the oxygen octahedral tilted [23] and they systematically appear only on the low-angle side of the Bragg peaks. (B) the broad and asymmetric diffuse regions of scattering is the most evident at around the Bragg peaks. These diffraction features are determined by the distorted nanoscale domain structures, which should result from the strain fields between ferroelastic domain walls [24].

We now study the ferroelastic microstructures in the (1-x)PZN-xPT (x = 0.07–0.11) single crystals. It is noteworthy that the relative position of the diffraction spots identifies the crystal structures, but the local lattice distortion and/or strain can be deduced from the shape of the diffraction spots. The unique ability of synchrotron μXRD is to characterize the reciprocal space lattice, which allows us to determine the spatial distribution of microstructure and strain in a manageable time frame. Therefore, we can use variations in the intensities of the

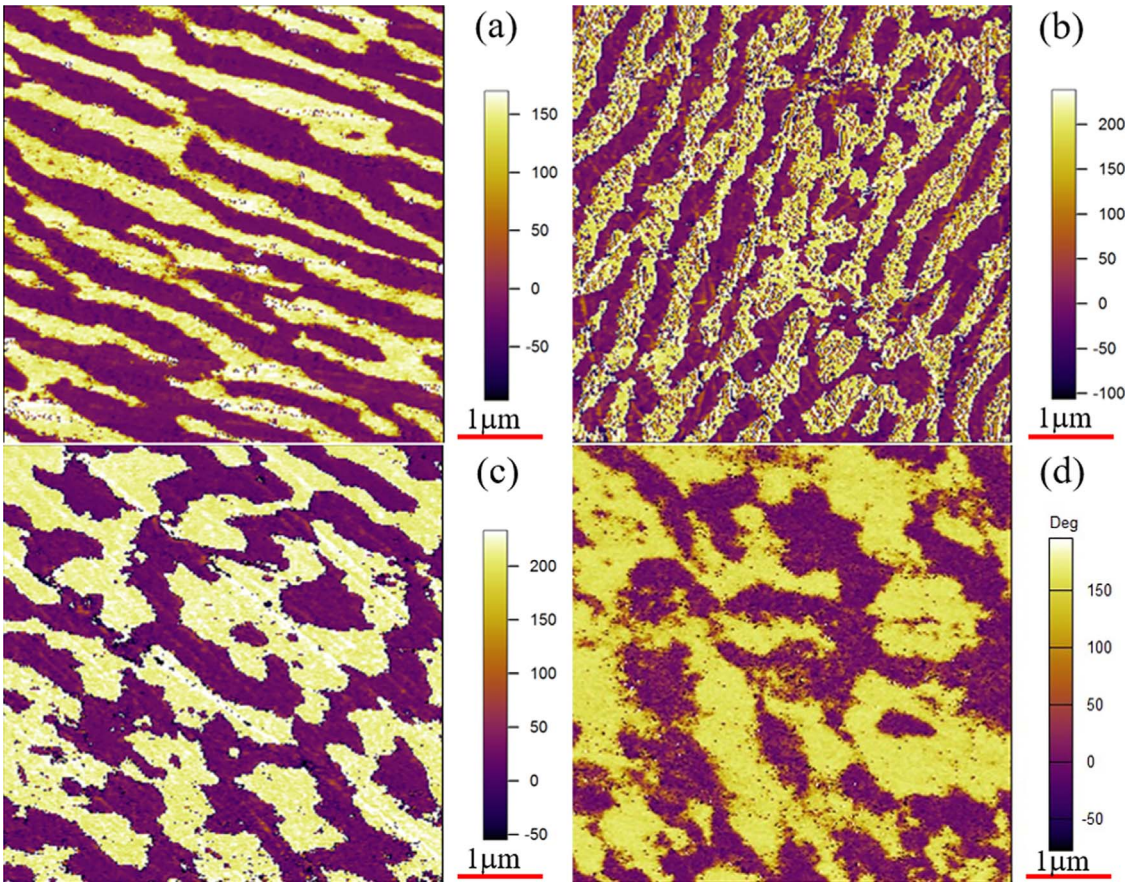

Fig. 3. Domain hierarchy of various $(001)_{pc}$-oriented (1-x)PZN-xPT (x = 0.07-0.11) single crystals for different compositions, (a): x = 0.07, (b): x = 0.08, (c): x = 0.09, and (d): x = 0.11.

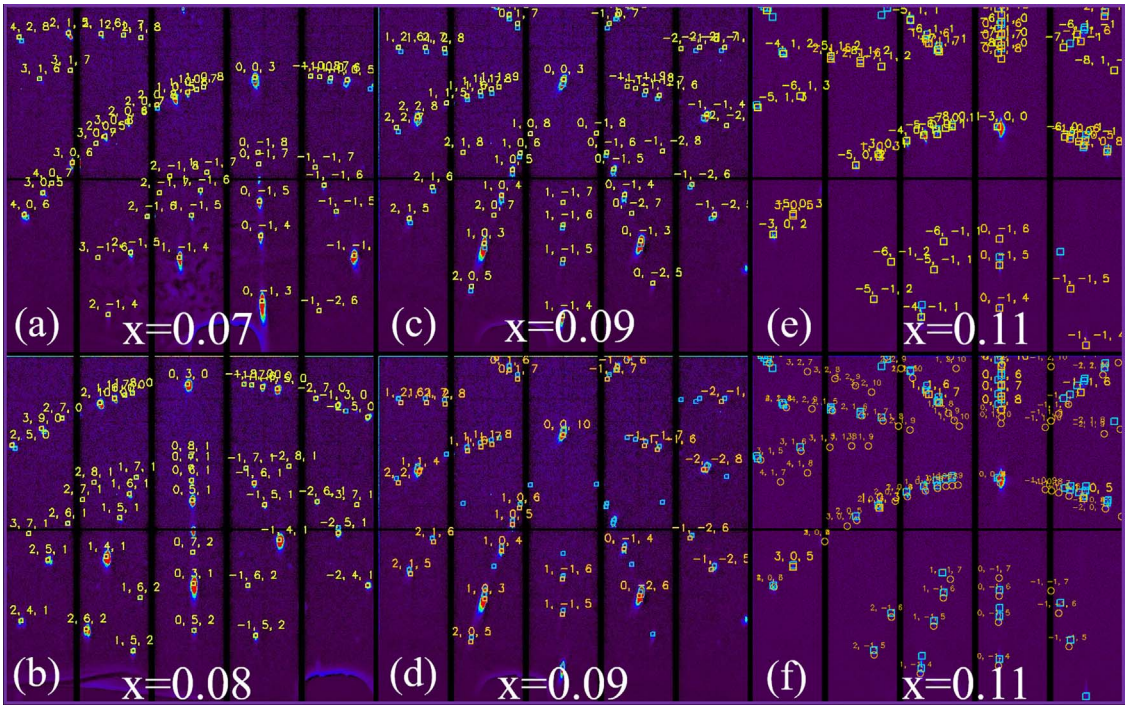

Fig. 4. White beam Laue diffraction patterns of the (1-x)PZN-xPT (x = 0.07-0.11) single crystals for different compositions, (a): x = 0.07, (b): x = 0.08, (c-d): x = 0.09, and (e-f): x = 0.11. (c): shows the indexed *O* phase spots, (d): shows the indexed *T* phase spots, (e): shows two different indexed *T* domains of their diffraction spots, and (f): shows one of the two *T* domains, the rotation angle of the two domains is determined as 0.5819°.

Table 1
Refinement results of synchrotron X-ray microdiffraction pattern of the (1-x)PZN-xPT (x = 0.07–0.09) single crystals at different temperatures, these patterns were fitted by XMAS software using least squared fitting method [18,19].

Composition	Temperature	Ferroelectric phase	lattice parameters
x = 0.07	27 °C	Orthorhombic phase	a = 4.043 Å, b = 4.064 Å, c = 4.070 Å
	80 °C	Monoclinic phase	a = 4.073 Å, b = 4.049 Å, c = 4.055 Å, β = 90.24°
	120 °C	Tetragonal phase	$a = b$ = 4.052 Å, c = 4.062 Å
x = 0.08	27 °C	Orthorhombic phase	a = 4.046 Å, b = 4.060 Å, c = 4.069 Å
	120 °C	Tetragonal phase	$a = b$ = 4.056 Å, c = 4.064 Å
	180 °C	Cubic and tetragonal phases existence	$a = b = c$ = 4.060 Å (*C*); $a = b$ = 4.051 Å, c = 4.062 Å (*T*)
x = 0.09	27 °C	Orthorhombic and tetragonal phases existence	a = 4.061 Å, b = 4.051 Å, c = 4.063 Å (*O*); $a = b$ = 4.056 Å, c = 4.063 Å (*T*)
	80 °C	Tetragonal phase	$a = b$ = 4.047 Å, c = 4.064 Å
	155 °C	Tetragonal phase	$a = b$ = 4.058 Å, c = 4.060 Å

split Laue peaks to represent the microstructure information. We must define a reciprocal space (*Q* space) coordinate system for these diffraction patterns. As shown in Fig. 4, the (0 0 3) or (0 3 0) diffraction spots can be used to define the Z- or Y-axes, which is normal to the sample surface. X-axis is defined as the direction connecting the (0 0 3) (or (0 3 0)) diffraction spot to the farthest diffraction spot along the (1–1 0) zone axis. We then integrate the intensity of the special diffraction spots in *Q* space along the [110] and [100] directions, which are the polarization directions of orthorhombic and tetragonal phases, respectively. This is for the purpose of a clear distinguish among orthorhombic phase, tetragonal phases, and their ferroelastic domains. Fig. 6(a–d) show the X-ray scattering profiles from a special (*hkl*) Bragg spot of the (1-x)PZN-xPT single crystals at room temperature under the above defined reciprocal space coordinate system. It can be clearly seen that the matrix peak presents an elliptical broadened scattering for the orthorhombic phase (samples of x = 0.07 and 0.08) (Fig. 6a and b). However, the irregular diffraction matrix peak was obtained from the samples of x = 0.09 and 0.11, with a mixture of ferroelectric phases (Fig. 6c and d). In particular, from Fig. 6d, it can be seen that the weak diffraction spot of the *O* phase located at the right of the strong diffraction *X*-shaped spot of the *T* phase. When the special spot was integrated, it is very interesting to observe that the diffraction peak of the *O* ferroelastic domain locates at the right of the *O* ferroelectric matrix (Fig. 6e–g), while the diffraction peak of *T* ferroelectric ferroelastic domain locates at the left of *T* ferroelectric matrix (Fig. 6g and h). It is worth noting that the diffraction peak width of ferroelastic domain phase in different crystal plane and different composition depends on the density of the ferroelastic domain variants, i.e., the more number of ferroelastic domain variants enables the more broadening of the diffraction peaks.

3.5. Ferroelastic domain observation by high-resolution transmission electron microscopy

Fig. 7(a) shows a typical dark-field TEM image illustrating the irregular hierarchical domains in the 0.93PZN-0.07PT crystal. The inset of Fig. 7(a) shows the high resolution twin lamella domains with a clear twin boundary. A schematic structural model for the ferroelastic twin

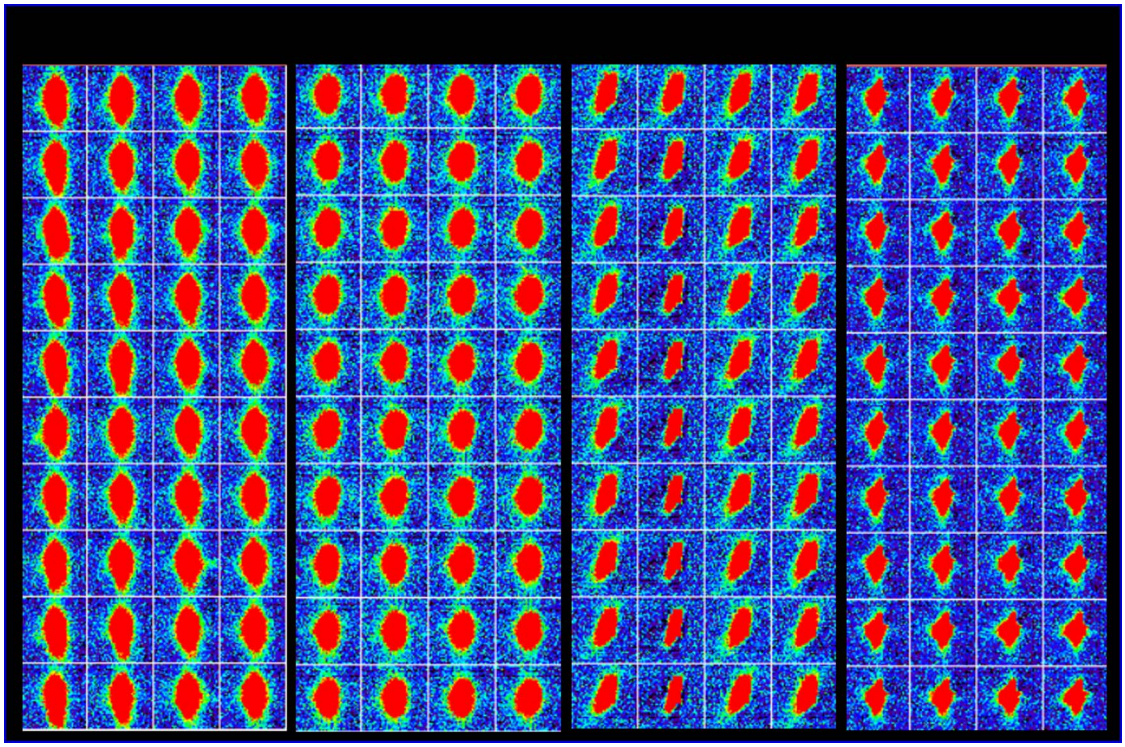

Fig. 5. An enlarged view of 40 $\{0\ 0\ l\}_{pc}$ diffraction spots taken from an area of 100 μm × 100 μm, showing highly uniformity in the (1-x)PZN-xPT ferroelectric single crystals. The x = 0.09 sample presents an obvious coexistence of *O* and *T* phases, as judged from the change of the full-width-at-half-maximum (FWHM) of diffraction spots.

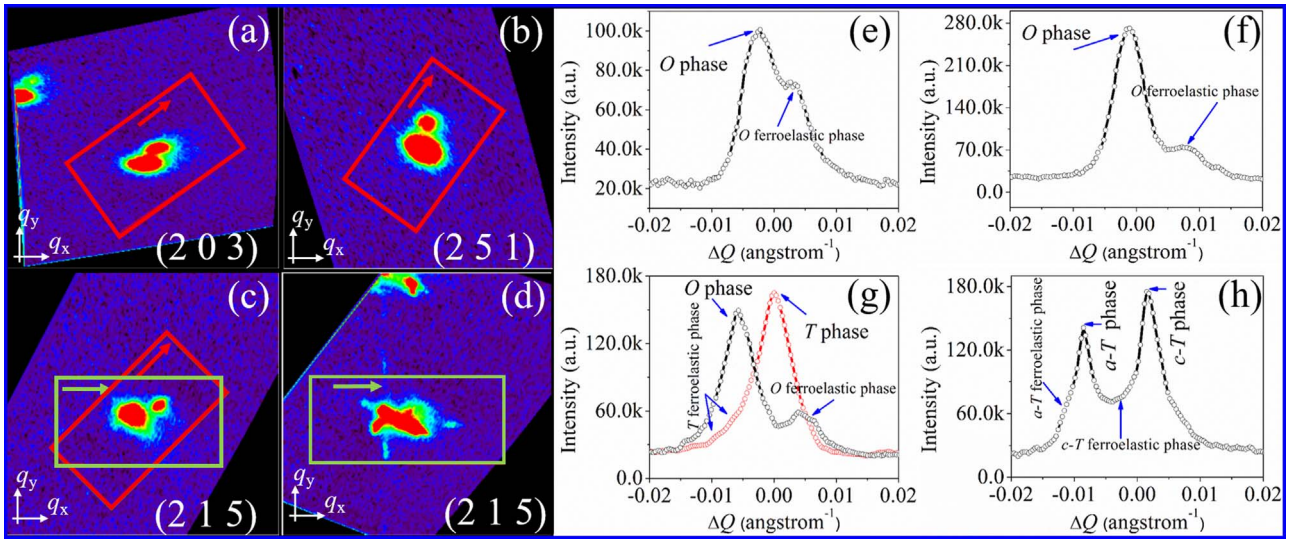

Fig. 6. Diffraction distribution in the *Q* space for the samples of different compositions, (a): (2 0 3) peak for $x = 0.07$, (b): (2 5 1) peak for $x = 0.08$, (c): (2 1 5) peak for $x = 0.09$, (d): (2 1 5) peak for $x = 0.11$. Images (e–h) are the integrated intensities of the tetragonal and orthorhombic phases along (1 0 0) and (1 1 0) directions, respectively. The red colored windows in (a–d) are the tetragonal integration windows. An olive colored window in (c) is the orthorhombic integration window. White arrows in (a–d) show the path of integration. (For interpretation of the references to colour in this figure legend, the reader is referred to the web version of this article.)

domains was drawn in Fig. 7(b). The selected area electron diffraction pattern (SAED) obtained from several twin domains shows the spot splitting along $[010]_{pc}$ direction, as shown in Fig. 7(c) and schematically illustrated in Fig. 7(d). The orthorhombic splitting angle in the present case that estimated from the electron diffraction is close to the calculated value of $\alpha = 2(\tan^{-1}(a/b)\text{-}45^{\circ}) \approx 0.3^{\circ}$, where *a* and *b* are lattice parameters of the *O* phase in the 0.93PZN-0.07PT sample. This splitting result from ferroelastic domain walls strain, which allows a slight domain distortion. The thickness of the ferroelastic domains is also dependence on the compositions, as shown in Fig. 8. It can be seen that the ferroelastic domain boundaries become more irregular, and the density of twin boundary also increases to a maximum at the composition of x = 0.09. Later on, the ferroelastic domain boundaries become regular with a lower density at the composition of x = 0.11.

3.6. Structural phase transitions in the (1-x)PZN-xPT single crystals by synchrotron μXRD

In order to understand the special phase transitions in the (1-x)PZN-xPT single crystals clearly (Fig. 2), we *in-situ* measured the local lattice distortions as a function of temperature using the scanning synchrotron μXRD in terms of deviations in unit cell parameters and atomic displacements relative to the centrosymmetric cubic structure (refined unite lattice parameters were listed in Table 1). Two unique structural phase transition sequences are deduced. One is that the structure of the x = 0.07 sample undergoes $O \rightarrow M \rightarrow T \rightarrow C$ phase transitions with increasing temperature. It should be noted that the *M* phase is an intermediate phase during the increase of temperature. No evidence of the existence of the *M* phase can be found at room temperature, which excludes the reason that the excellent piezoelectric response of PZN-PT

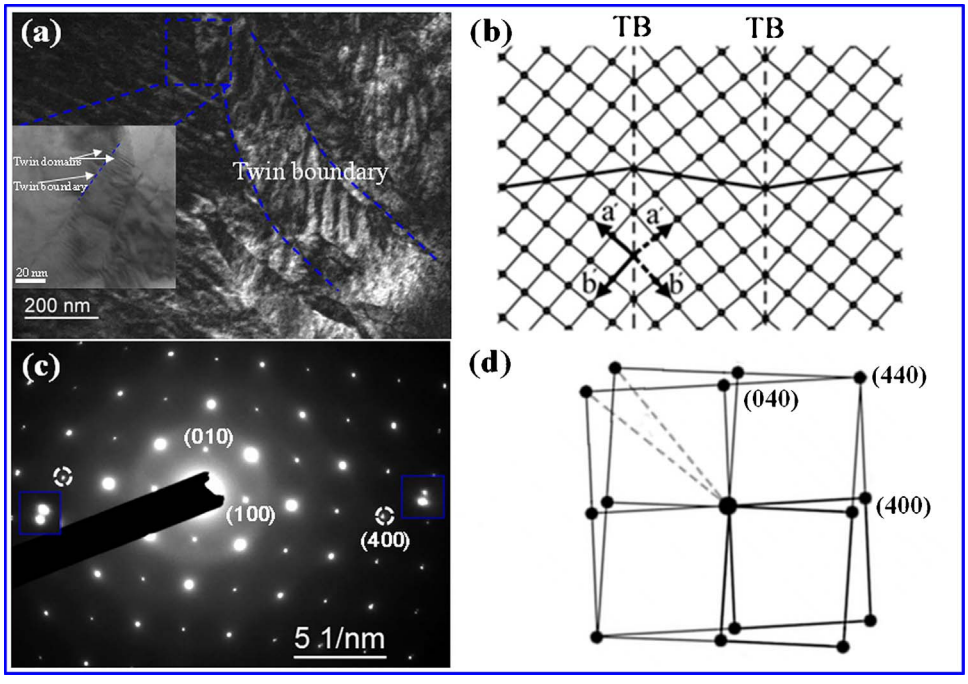

Fig. 7. (a): A typical dark-field TEM image of the 0.93PZN-0.07PT single crystal. (b): Schematic representation of a structural model showing the ferroelastic domain structure in 0.93PZN-0.07PT crystal. Where TB denotes ferroelastic domain boundary and a′ (or b′) are parallel to the $[100]_{pc}$ ($[010]_{pc}$) directions in the orthorhombic phase. (c): The SAED obtained from the area shown in (a). The marked features (i.e. square boxes) of (c) show enlarged (4 0 0)/(−4 0 0) Bragg spots with unambiguous spot splitting. (d): Schematic illustration of splitting of the electron diffraction spots resulted from the ferroelastic structure.

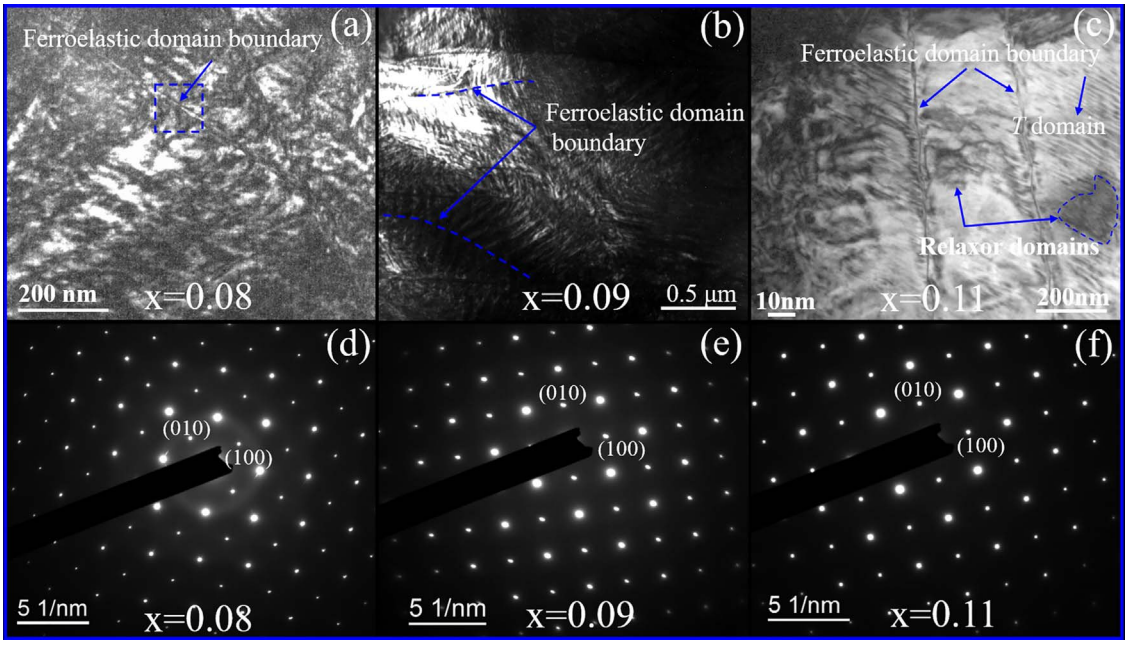

Fig. 8. Dark field ferroelectric domain images of the (1-x)PZN-xPT single crystal for different compositions, (a): x = 0.08, (b): x = 0.09, (c): x = 0.11, and (d-f): show the SAED patterns corresponding to (a-c), respectively.

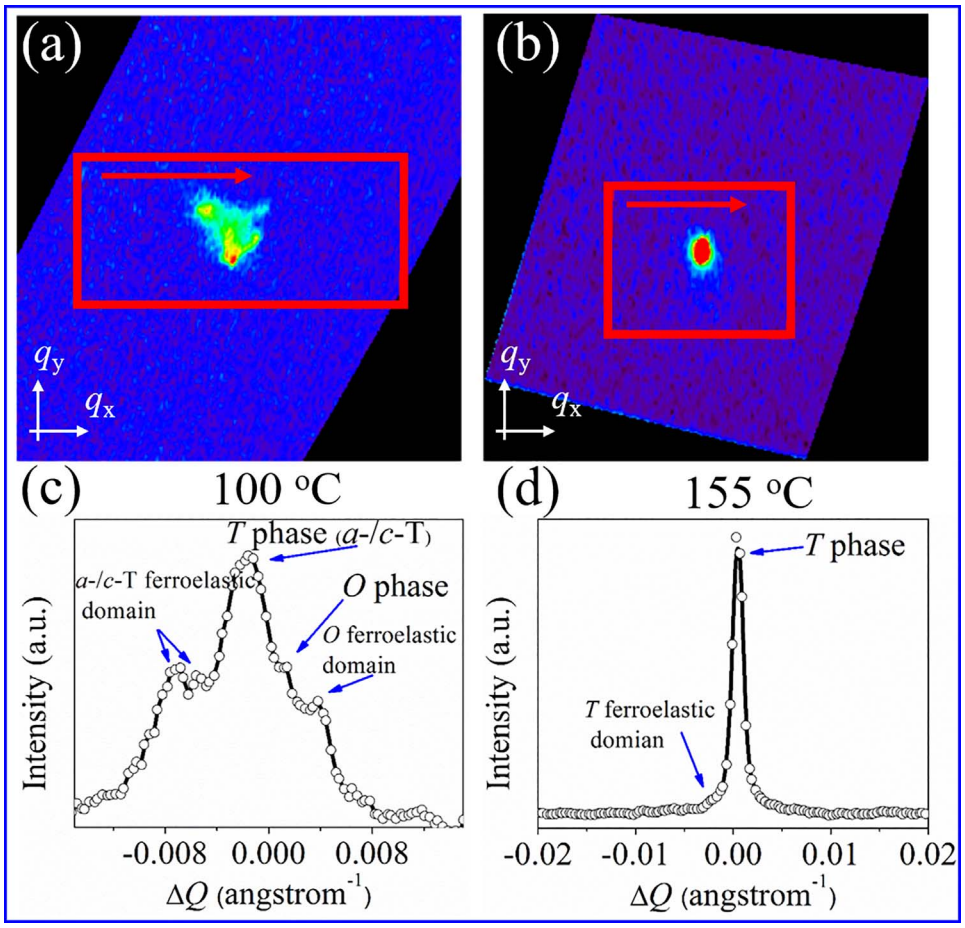

Fig. 9. Temperature dependence of the (2 1 5) diffraction distribution in *Q*-space for the x = 0.09 sample at (a): 100 °C and (b): 155 °C. (c–d): Integrated intensities of the tetragonal and orthorhombic phases along [100] and [110] direction, respectively. The red colored windows in (a-b) are due to the tetragonal phase integration. The red colored arrows show the path of integration. (For interpretation of the references to colour in this figure legend, the reader is referred to the web version of this article.)

is due to the *M* phase. The other is that, for the x = 0.09 sample, there is no evidence of a structural phase transition in a range of 130–165 °C, indicating a phase transition sequence of $O + T \rightarrow T \rightarrow C$. This unique phase transition in the x = 0.09 sample is intimately related to the evolution of multifold nanoscale ferroelastic domains with an increasing temperature, which results a dielectric anomaly observed at ~155 °C (as shown in Fig. 2). The evidence is shown in Fig. 9 (a)–(d), combined with Fig. 6(c) and (e) results, it is found that the coexistence

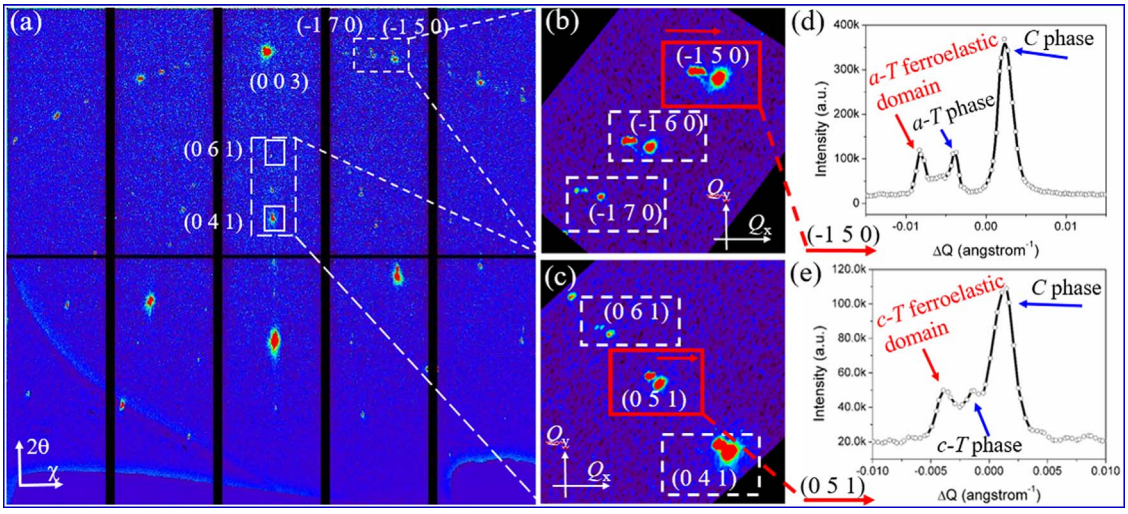

Fig. 10. (a): White beam Laue diffraction pattern of the 0.92PZN-0.08PT single crystal at 180 °C. (b and c): Enlarged *Q*-space images of some diffraction spots from [001] and [100] zone-axes. Red colored rectangular boxes and their corresponding arrow marks show the integration window and the path of integration, respectively. (d and e): Profiles of the (−1 5 0) and (0 5 1) diffraction peaks plotted as a function of reciprocal vector along [100] direction. (For interpretation of the references to colour in this figure legend, the reader is referred to the web version of this article.)

of the *O* and *T* phases gradually transforms into the *T* phase, which can be seen from the evolution of the (2 1 5) spots with an increasing temperature. Meanwhile, the ferroelastic domains of *O* and *T* phases transformed into ferroelastic domain of *T* phase. Another important observation is that the ferroelectric tetragonal and paraelectric cubic phases coexist in the x = 0.08 sample at 180 °C (above the Curie temperature ~15 °C), which is in consistent with the observation by Kisi et al. [20]. As shown in Fig. 10, the most diffraction spots split along the 2θ direction (Fig. 10a), and the *Q*-space enlarged images (Fig. 10b and c) of the diffraction spots from [001] and [100] zone-axes show simultaneous presence of the paraelectric cubic and the polar ferroelectric *T* phases. The diffraction spots (for example, (−1 5 0) and (0 5 1) spots in Fig. 10b and c) of the cubic phase are sharp with isotropic scattering. This is because of polarization vector is near to zero accompanied with polar nano regions (PNRs). The tetragonal phase has *c*- and *a*-domains that are parallel and perpendicular to [001] direction. Therefore, there are two diffraction spots for polar ferroelectric *T* phase located on left of *C* phase diffraction, as shown in Fig. 10d and e. They split along the reciprocal vector direction Q_x or Q_y due to the $[001]_{pc}$ polarization-led symmetry breaking, indicating that the formation of {1 1 0}-type *T* ferroelastic domain walls. Alternatively, at the high temperature of 180 °C, the (−1 5 0) diffraction spot (Fig. 10d) shows the *a*-ferroelastic *T* domain, which own two kind of orientations (i.e. poled axes parallel to Q_x and Q_y). The ferroelastic domains of *a*-*T* domain presented a broaden feature, which is because of the tilted angle between inside and boundary of ferroelastic domains own tilted gradient. However, the (0 5 1) diffraction shows the ferroelastic domains of *c*-*T* domain diffractions (Fig. 10e), formatting to a broadened twin peak. Therefore, by combining the above results with previous works [13,25,26], we add the ferroelastic domain structure into the phase diagram of PZN-PT near the MPB, as shown in Fig. 11.

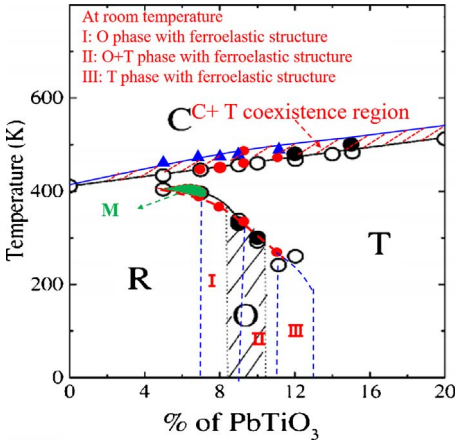

Fig. 11. Revised phase diagram of PZN-PT around its MPB. The open circles and solid lines represent the phase diagram by Kuwata et al. (see Ref. [25]). The blue line and triangle represent the phase diagram by Chang et al. (see Ref. [26]). The black solid circle and shaded area represent the phase diagram by La-Orauttapong et al. (see Ref. [13]). The results of this present work are plotted as red solid circles and red dashed lines. The orthorhombic phase (*O*) ferroelastic structure is represented separately by blue dashed lines and the new *M* phase is shown in the green colored area. (For interpretation of the references to colour in this figure legend, the reader is referred to the web version of this article.)

3.7. Thermally activated domain evolution in the (1-x)PZN-xPT (x = 0.07–0.11) single crystals

X-ray microdiffraction patterns were collected from the (1-x)PZN-xPT single crystals as a function of temperature. When the samples were heated from room temperature to above the Curie temperature, the super-structured diffraction spots gradually become more and more sharper, and finally converge into one, indicating that an increased domain size and relaxed strain fields of ferroelastic domain walls, as shown in Fig. 12. Above the T_C, the diffraction spots keep asymmetric due to the coexistence of polar ferroelectric *T* phase. Compared with the x = 0.07 and 0.08 samples, the diffraction patterns of 0.91PZN-0.09PT under various temperatures present a slight weaker diffuse feature that is due to the larger polar domain size. It can be observed clearly from the (2 1 5) diffraction spot of x = 0.09 that the ferroelectric *O* phase gradually transforms into ferroelectric *T* phase with an increasing temperature. For the x = 0.11 sample, the complicated domain structure consists of tetragonal ferroelastic domains and some minor orthorhombic domains. At 50 °C, the (−1 0 6) and (−1 0 7) diffraction spots from the *O* and *T* phases are separated clearly, due to increased domain size with an increasing temperature. *X*-shaped diffraction spot originates from intensity variation of the *a*-/*c*-*T* domains as well as their ferroelastic domain variants. It is worth noting that the *O* phase structure (in the x = 0.11 sample) disappeared and transformed into *T* phase completely at 80 °C.

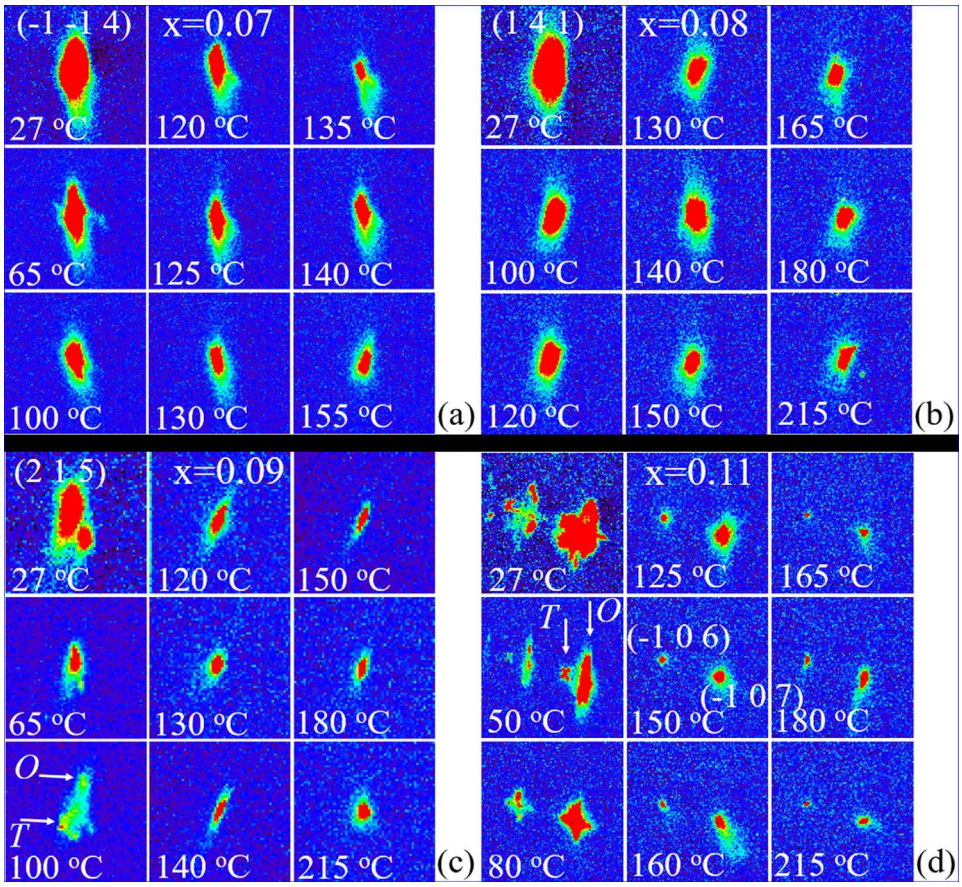

Fig. 12. Temperature dependence of the diffraction spots in the (1-x)PZN-xPT single crystals illustrating the evolution of ferroelectric domains, (a): (−1 −1 4) spot of the x = 0.07 sample, (b): (1 4 1) spot of the x = 0.08 sample, (c): (2 1 5) spot of the x = 0.09 sample, and (d): (−1 0 6) and (−1 0 7) spots of the x = 0.11 sample.

4. Conclusions

The structural phase transformations and nanoscale ferroelastic domain structures in the (1-x)PZN-xPT (x = 0.07–0.11) single crystals were discussed based on *in-situ* synchrotron white-beam X-ray microdiffraction (μXRD) results as well as their complementary HR-TEM and PFM measurements. It is found that, at room temperature the (1-x)PZN-xPT single crystals with x = 0.07–0.08 are ferroelectric *O* phase, the x = 0.09 sample consists of a mixture of *O* and *T* phases, and the x = 0.11 sample consists of a *T* phase with a minor *O* phase. The ferroelectric domains accompanied by the ferroelastic domains near the MPB compositions. Upon heating, the phase transformation path in 0.93PZN-0.07PT is Orthorhombic → Monoclinic → Tetragonal → Cubic. The coexistence of ferroelectric tetragonal and paraelectric cubic phases was *in-situ* observed in 0.92PZN-0.08PT above Curie temperature (T_C), indicating an order-disorder phase transition in the PZN-PT single crystals. The evolution of ferroelectric domain and ferroelastic domain results in the abnormal dielectric phase transition of (1-x)PZN-xPT single crystals. This finding provides new clues to the understanding of the microstructure and phase transition of the PZN-PT relaxor ferroelectric single crystals.

Acknowledgments

This work was supported by the Research Grants Council of the Hong Kong Special Administrative Region, China (Project No. PolyU152665/16E) and the Hong Kong Polytechnic University (1-ZVGH). It was also supported by the Hong Kong, Macao and Taiwan Science & Technology Cooperation Program of China (No. 2015DFH10200), the Science and Technology Research Items of Shenzhen (No. JCYJ20160422102802301 and KQJSCX2016022619562452), the Chinese Postdoctoral Science Foundation (No. 2015M572356), and the National Natural Science Foundation of China (No. 11604214). The experiments in the Advanced Light Source at the Lawrence Berkeley National Laboratory was supported by the Office of Science, Office of Basic Energy Sciences, and Scientific User Facilities Division of the U.S. Department of Energy under Contract No. DE-AC02-05CH11231.

References

[1] S.J. Zhang, F. Li, X. Jiang, J. Kim, J. Luo, X. Geng, Advantages and challenges of relaxor-$PbTiO_3$ ferroelectric crystals for electroacoustic transducers—a review, Prog. Mater. Sci. 68 (2015) 1–66.
[2] E.W. Sun, W.W. Cao, Relaxor-based ferroelectric single crystals: Growth, domain engineering, characterization and applications, Prog. Mater. Sci. 65 (2014) 124–210.
[3] H.X. Fu, R.E. Cohen, Polarization rotation mechanism for ultrahigh electromechanical response in single-crystal piezoelectrics, Nat 403 (2000) 281–283.
[4] R. Guo, L.E. Cross, S.-E. Park, B. Noheda, D.E. Cox, G. Shirane, Origin of the high piezoelectric response in $PbZr_{1-x}Ti_xO_3$, Phys. Rev. Lett. 84 (2000) 5423–5426.
[5] D. Viehland, Symmetry-adaptive ferroelectric mesostates in oriented $Pb(BI_{1/3}BII_{2/3})O_3$-$PbTiO_3$ crystals, J. Appl. Phys. 88 (2000) 4794–4806.
[6] Y.M. Jin, Y.U. Wang, A.G. Khachaturyan, J.F. Li, D. Viehland, Conformal miniaturization of domains with low domain-wall energy: monoclinic ferroelectric states near the morphotropic phase boundaries, Phys. Rev. Lett. 91 (2003) 197601.
[7] Y.M. Jin, Y.U. Wang, A.G. Khachaturyan, J.F. Li, D. Viehland, Adaptive ferroelectric states in systems with low domain wall energy: tetragonal microdomains, J. Appl. Phys. 94 (2003) 3629–3640.
[8] Y.U. Wang, Diffraction theory of nanotwin superlattices with low symmetry phase, Phys. Rev. B 74 (2006) 104109.
[9] Y.U. Wang, Diffraction theory of nanotwin superlattices with low symmetry phase: application to rhombohedral nanotwins and monoclinic M_A and M_B phases, Phys. Rev. B 76 (2007) 024108.
[10] B. Noheda, D.E. Cox, G. Shirane, S.-E. Park, L.E. Cross, Z. Zhong, Polarization rotation via a monoclinic phase in the piezoelectric 92% $Pb(Zn_{1/3}Nb_{2/3})O_3$-8% $PbTiO_3$, Phys. Rev. Lett. 86 (2001) 3891–3894.
[11] Z.G. Ye, B. Noheda, M. Dong, D.E. Cox, G. Shirane, Monoclinic phase in the relaxor-based piezoelectric/ferroelectric $Pb(Mg_{1/3}Nb_{2/3})O_3$-$PbTiO_3$ system, Phys. Rev. B 64 (2001) 184114.
[12] D.E. Cox, B. Noheda, G. Shirane, Universal phase diagram for high-piezoelectric perovskite systems, Appl. Phys. Lett. 79 (2001) 400–402.
[13] D. La-Orauttapong, B. Noheda, Z.G. Ye, P.M. Gehiring, J. Toulouse, D.E. Cox, G. Shirane, Phase diagram of the relaxor ferroelectric (1-x)$Pb(Zn_{1/3}Nb_{2/3})O_3$-

xPbTiO$_3$, Phys. Rev. B 65 (2002) 144101.
[14] H. Wang, J. Zhu, N. Lu, A.A. Bokov, Z.G. Ye, Hierarchical micro-/nanoscale domain structure in M_C phase of (1-x)Pb(Mg$_{1/3}$Nb$_{2/3}$)O$_3$-xPbTiO$_3$ single crystal, Appl. Phys. Lett. 89 (2006) 042908.
[15] S. Bhattacharyya, J.R. Jinschek, H. Cao, Y.U. Wang, J.F. Li, Direct high-resolution transmission electron microscopy observation of tetragonal nanotwins within the monoclinic M_C phase of Pb(Mg$_{1/3}$Nb$_{2/3}$)O$_3$-0.35PbTiO$_3$ crystals, Appl. Phys. Lett. 92 (2008) 142904.
[16] T. Li, X.F. Long, High-performance ferroelectric solid solution crystals: pb(In$_{1/2}$Nb$_{1/2}$)O$_3$-Pb(Zn$_{1/3}$Nb$_{2/3}$)O$_3$-PbTiO$_3$, J. Am. Ceram. Soc. 97 (2014) 2850–2857.
[17] F. Li, L.H. Wang, L. Jin, Z. Xu, S.J. Zhang, Achieving single domain relaxor-PT crystals by high temperature poling, CrystEngComm 16 (2014) 2892–2897.
[18] N. Tamura, R.S. Celestre, A.A. MacDowell, H.A. Padmore, Submicron x-ray diffraction and its applications to problems in materials and environmental science, Rev. Sci. Instrum. 73 (2002) 1369–1372.
[19] N. Tamura, R. Barabash, G. Ice (Eds.), Strain and Dislocation Gradients from Diffraction: Spatially Resolved Local Structure and Defects, Imperial College Press, Singapore, 2014, pp. 125–155.
[20] E.H. Kisi, J.S. Forrester, The phase transition sequence in the relaxor ferroelectric PZN-8% PT, J. Phys.: Condens. Matter 20 (2008) 165208.
[21] F.M. Bai, J.F. Li, D. Viehland, Domain hierarchy in annealed (001)-oriented Pb(Mg$_{1/3}$Nb$_{2/3}$)O$_3$-xPbTiO$_3$ single crystals, Appl. Phys. Lett. 85 (2004) 2313–2315.
[22] B. Noheda, D.E. Cox, J. Shirane, Z.-G. Ye, J. Gao, Phase diagram of the ferroelectric relaxor (1-x)Pb(Mg$_{1/3}$Nb$_{2/3}$)O$_3$-xPbTiO$_3$, Phys. Rev. B 66 (2002) 054104.
[23] J.M. Kiat, Y. Uesu, B. Dkhil, M. Matsuda, C. Malibert, G. Calvarin, Monoclinic structure of unpoled morphotropic high piezoelectric PMN-PT and PZN-PT compounds, Phys. Rev. B 65 (2002) 064106.
[24] D. Dragan, Comments on origins of enhanced piezoelectric properties in ferroelectrics, IEEE transactions on ultrasonics, ferroelectrics, IEEE Trans. Ultrason. Ferroelect. Freq. control 56 (2009) 1574–1585.
[25] J. Kuwata, K. Uchino, S. Nomura, Phase transition in Pb(Zn$_{1/3}$Nb$_{2/3}$)O$_3$-PbTiO$_3$ system, Ferroelectrics 37 (1981) 579–582.
[26] W.-S. Chang, High-resolution X-ray diffraction study of phase and domain structures in relaxor ferroelectric crystals, Scholarbank@NUS, 2009. http://scholarbank.nus.edu.sg/handle/10635/16831.